AD-A156 425 PREDICTION OF PLASTICITY CHARACTERISTICS FOR THREE-DIMENSIONAL FRACTURE S..(U) GEORGE WASHINGTON UNIV WASHINGTON DC SCHOOL OF ENGINEERING AN.. 1/1

UNCLASSIFIED E T MOYER JR. ET AL. 1985 N00014484-K-0027 F/G 11/9 NL

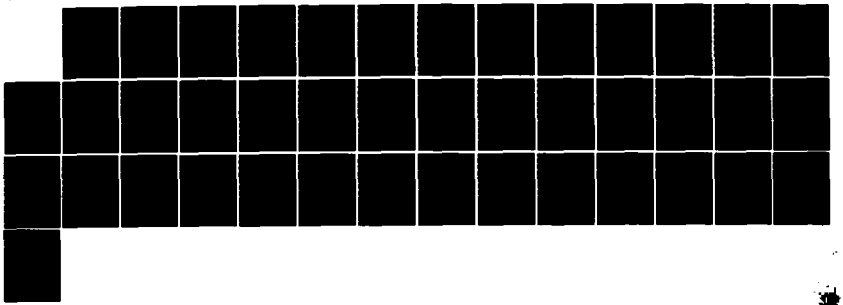

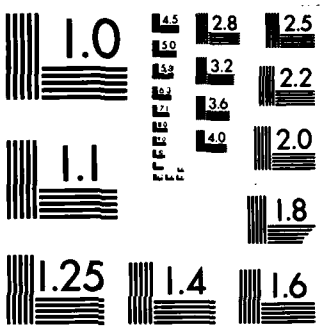

MICROCOPY RESOLUTION TEST CHART
NATIONAL BUREAU OF STANDARDS-1963-A

(12)

PREDICTION OF PLASTICITY CHARACTERISTICS FOR THREE-DIMENSIONAL FRACTURE SPECIMENS COMPARISON WITH EXPERIMENT

By

E. T. Moyer, Jr.
P. K. Poulose
H. Liebowitz

Contract N00014-84-K-0027

1985

The School of Engineering and Applied Science
The George Washington University
Washington, D.C. 20052

ABSTRACT

A center-cracked panel of 7075-Aluminum alloy which has overaged from the T651 condition was loaded in tension and subsequently unloaded to zero applied load. The permanent surface deformation was measured close to the intersections of the crack front with the free surfaces. The permanent deformation (being a good indicator of the extent of plastic deformation) was used to measure the accuracy of finite element analyses.

The same specimen was modeled using 20-node three-dimensional isoparametric elements. A fully incremental elastic-plastic formulation was employed in the stress analysis. The residual surface deformations after unloading were compared to the experimental results.

The average experimental results compare quite favorably with the finite element predictions. The average results were employed to minimize the influence of material inhomogeneity, load misalignment, and lack of symmetry in the fatigue crack. The scatter in the results from measuring the different sides is discussed.

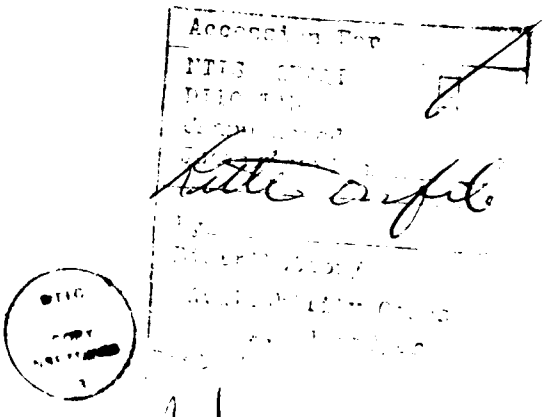

INTRODUCTION

Over the past 35 years, the field of fracture mechanics has evolved and developed into an important and useful tool for the design of engineering components and structures. Several major problems dealing with the criticality of cracks in engineering components and structures can now be answered with great accuracy. Specifically, problems involving straight cracks in brittle materials undergoing Mode I deformation only can be accurately predicted. Most problems which occur in practice, however, involve materials which are ductile in the loading applications for which they are employed. Many cracks are also initiated in sites which involve complicated loading which involve more than a single fracture mode. Finally, most problems arising in application involve geometries which can not be accurately approximated two-dimensionally. The major research in fracture mechanics today, therefore, is geared toward addressing the issues of ductility, mixed-mode loading and three-dimensionality.

The issue of plasticity and ductility in fracture specimens has long been a concern of researchers. Many attempts have been made to propose fracture criteria which account for ductility and to develop numerical tools to perform stress analyses. The development and refinement of the finite element method has

greatly aided the progress in this area. Many two-dimensional studies have been performed using elastic-plastic finite element modeling. While much of the early work has been demonstrated erroneously, several accurate computational procedures are now available. The area of failure prediction has not been as successful as the area of stress analysis. No viable ductile fracture criteria have been proposed which pass the tests of specimen and geometry independence, consistent and theoretically sound formulation, and reproducibility. The best that can be said for the existing criteria is that for limited realms of applicability (usually vary within 10-15% of the range of brittle criteria), the proposed methods offer conservative estimates for failure loads which are not as strict as the brittle predictions. It is important to recognize at the outset that elastic-plastic fracture parameters (e.g., J-integral, CTOD, CMOD, etc.) can either be shown to be theoretically invalid for true plasticity problems, or, are simply experimental observations which not do pass the test of specimen and geometry independence.

During the past three years, the authors have focused their research on addressing the three-dimensional aspects of ductile fracture. A major first step has been the development of an accurate and theoretically consistent computational approach to the stress analysis of three-dimensional fracture specimens. In

a series of recent papers [1,2,3], the effect of specimen thickness, material hardening characteristics and mesh characteristics have been investigated. These results give much insight into the necessary properties for ductile fracture criteria. While no new criteria have emerged to date (either from the authors or others), the groundwork for analyzing and assessing criteria has been established.

A major problem with ductile fracture problems in three-dimensions is the establishment of the accuracy of the analysis. Convergence studies are extremely costly and only show the consistency of the approach. They in no way guarantee agreement with the behavior of real materials. To address this problem, the study presented in this paper compares the deformation predicted from a full three-dimensional incremental plasticity finite element analysis to the deformations measured in the laboratory. A center-cracked panel was chosen for the study for two reasons: first, the authors' previous studies have been performed on center-cracked panels and second, the specimen is easier to model with finite elements as the effects of the loading holes are easier to account for (by using an accurate gauge length). While a successful comparison does not guarantee the accuracy of any given study other than the present, it is the most rigorous way of establishing the validity of the approach and demonstrating the qualitative agreement of the predictions made previously with the behavior of real fracture specimens.

ELASTIC-PLASTIC FINITE ELEMENT FORMULATION

The stress analysis in this study is performed utilizing the finite element method to solve the basic elastic-plastic governing equations for the deformation of continuum solids. J_2 flow theory plasticity is employed with the standard associative flow law. The Newton-Raphson, or Tangent-Stiffness approach is employed in the finite element formulation to handle nonlinearities. The Updated Lagrangian coordinate system is employed to handle finite strains. The formulation of all equations is outlined in this section.

The J_2 flow theory of plasticity assumes that the material in question yield, or starts deforming plastically when the "effective stress" (or von-Mises stress) reaches a critical value (called the yield stress). Prior to the onset of plasticity, the material is assumed to behave linear elastically. Subsequently, the deviatoric stress components are related to the deviatoric strain rate through the tensor relation

$$\dot{e}_{ij} = \begin{cases} \frac{1+\nu}{E}\dot{S}_{ij} + \frac{3}{Z} f(\sigma_e)\, S'_{ij}\, \dot{\sigma}_e & \left[\begin{matrix}\sigma'_e = R_{yd} \\ \dot{\sigma}_e > 0\end{matrix}\right] \\ \frac{1+\nu}{E}\dot{S}_{ij} \quad \text{(otherwise)} & \end{cases} \tag{1}$$

where $\dot{e}_{ij}$ are the deviatoric strain rates given by

$$\dot{e}_{ij} = \dot{\varepsilon}_{ij} - \frac{1}{3} \dot{\varepsilon}_{pp} \delta_{ij} \tag{2}$$

S_{ij} are the current deviatoric stress components given by

$$S_{ij} = \sigma_{ij} - \frac{1}{3} \sigma_{pp} \delta_{ij} \tag{3}$$

S'_{ij} are the deviatoric stress components measured relative to the current yield surface center given by

$$S'_{ij} = S_{ij} - a_{ij} \tag{4}$$

a_{ij} are the coordinates in stress space of the current yield surface center, σ_{ij} are the Cauchy stress components, ε_{ij} are the "true" strain components (discussed in a subsequent section), σ_e is the effective stress given by

$$\sigma_e = \sqrt{\frac{3}{2} S_{ij} S_{ij}} \tag{5}$$

and σ'_e is the effective stress measured relative to the current yield surface center

$$\sigma'_e = \sqrt{\frac{3}{2} S'_{ij} S'_{ij}} \quad . \tag{6}$$

The function $f(\sigma_e)$ is derived from the uniaxial stress-strain curve and is consistent with the Associated Plasticity Theory (a complete discussion is given in Reference [4]). Derivation of $f(\sigma_e)$ for a multilinear representation of the stress-strain curve will be discussed subsequently.

For plastic strains which are incompressible, the hydrostatic plastic strain rate is zero. The total hydrostatic strain rate, therefore, is related to the related to the hydrostatic stress rate by

$$\dot{\epsilon}_{pp} = \frac{1 - 2\nu}{E} \dot{\sigma}_{pp} \tag{7}$$

Engineering materials exhibit different types of uniaxial hardening behavior when subsequently unloaded after being plastically deformed. Generally, the behavior falls between two extremes called kinematic and isotropic hardening. The uniaxial representation of these behaviors for a bilinear material are shown in Figure 1. To allow for various hardening behaviors in the multiaxial formulation, the yield surface is permitted to move and expand under certain constraints. These motions are controlled by a single parameter, β, which can be varied from 0 to 1. A value of zero represents isotropic behavior and a value of 1 represents kinematic behavior. The resulting yield surfaces in a three-dimensional principle stress space are shown in Figure 2. The yield surface center moves at a rate governed by

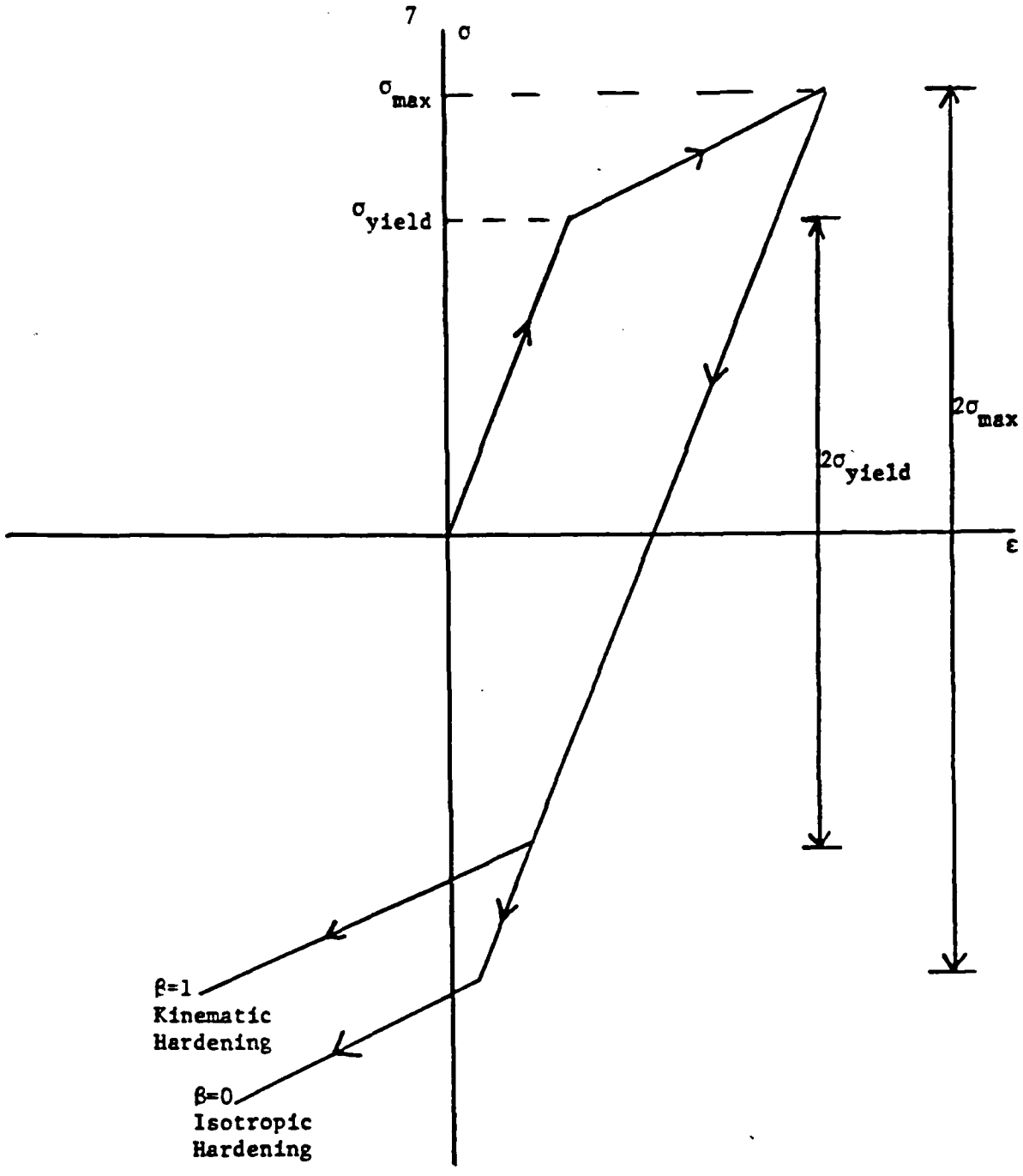

Figure 1: Uniaxial Bilinear Representation of Kinematic and Isotropic Hardening.

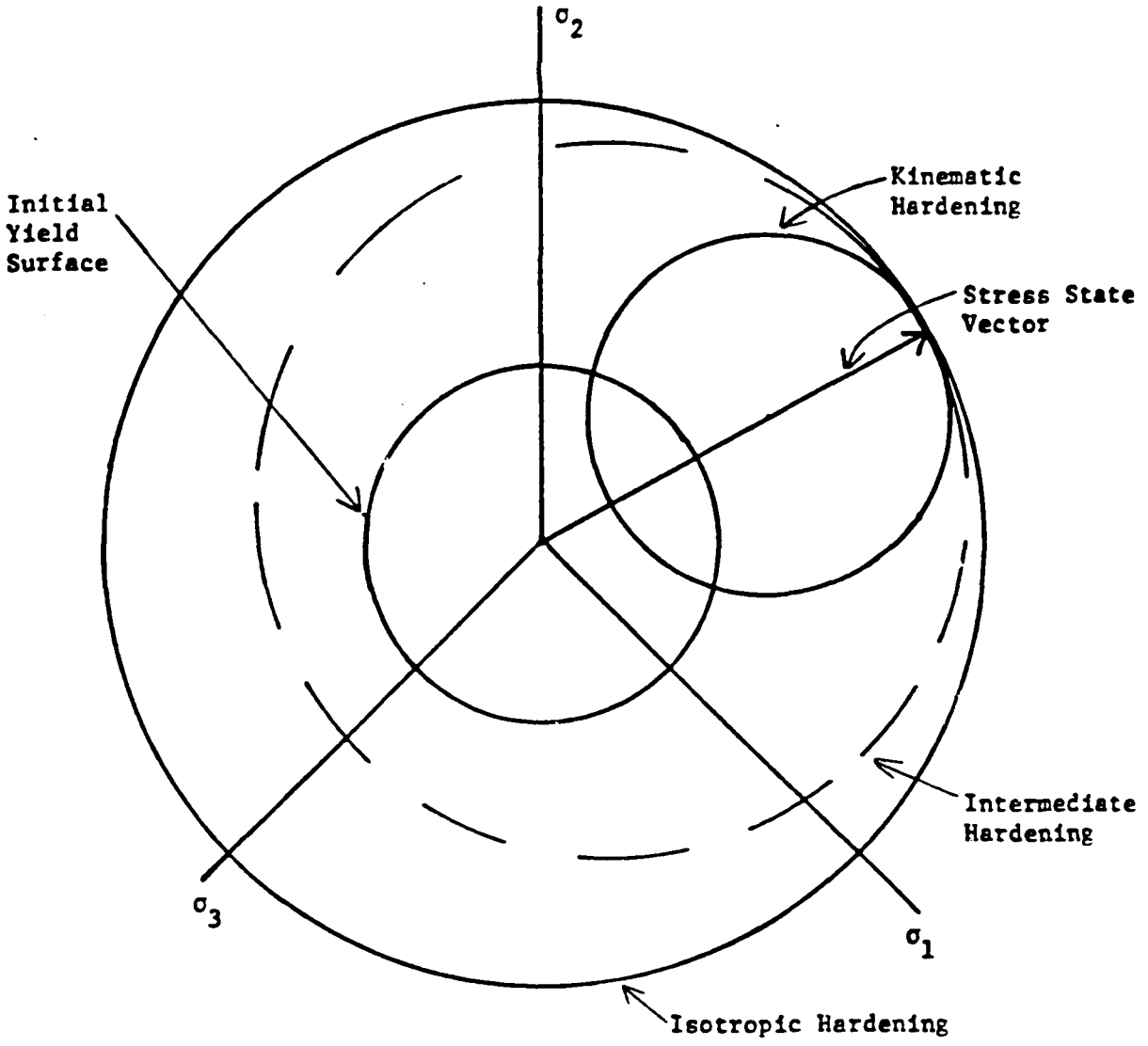

Figure 2: Hardening Models in Principle Stress Space.

$$\dot{a}_{ij} = \begin{cases} \frac{3}{Z}\beta S'_{kl}\dot{S}_{kl}S'_{ij}/(\sigma'_e)^2 & \left[\sigma'_e = \sigma_{yd},\ \dot{\sigma}_e > 0\right] \\ 0 \text{ (otherwise)} & \\ 0 \leq \beta \leq 1 & \end{cases} \tag{8}$$

$\beta = 0 \rightarrow$ Isotropic Hardening

$\beta = 1 \rightarrow$ Kinematic Hardening

$$\sigma'_y = 2\sigma_y + 2\beta(\sigma_{max} - \sigma_y) \tag{9}$$

To allow for finite strains and rotations, Updated Lagrangian approach is adopted [5]. The coordinate system is convected with the deformation. In this coordinate system, the "true strain" rate is related to the determination rate (or velocity) through

$$\dot{\sigma}_{ij} = C_{ijkl}\dot{\epsilon}_{kl} \tag{10}$$

In the absence of rotation the stress tensor is related to the strain rate tensor in the classical manner, i.e.,

$$\dot{W}_{ij} = \frac{1}{2}\left(\frac{\partial \dot{U}_i}{\partial X_j} - \frac{\partial \dot{U}_j}{\partial X_i}\right) \tag{11}$$

This stress measure is the Cauchy stress. Under finite rotations, the stress tensor is not invariant. At zero strain rate, the stress rate is given by where W are the rotation rates

$$\dot{\sigma}_{ij} = \dot{W}_{ip}\,\sigma_{pj} - \dot{W}_{pj}\,\sigma_{ip} \tag{12}$$

The total stress-deformation relation is, therefore,

$$\dot{\sigma}_{ij} = C_{ijkl}\,\dot{\varepsilon}_{kl} + \dot{W}_{ik}\,\sigma_{kj} - \dot{W}_{kj}\,\sigma_{ik} \tag{13}$$

Equations (1) - (13) form a complete incremental representation of finite plastic deformation. It only remains, therefore, to quantify the uniaxial behavior through the function $f(\sigma_e)$. There are many functional ways to represent uniaxial loading behavior. From a computation standpoint, a multilinear representation is easily implemented and, by allowing for enough segments, can be arbitrarily accurate. Consider the multilinear representation of a true stress-true

strain curve shown in Figure 3. The functional relationship between the stress and strain are given by

$$\varepsilon = \frac{\sigma}{E} + \frac{\alpha_1}{E}(\sigma_2 - \sigma_1) + \frac{\alpha_2}{E}(\sigma_3 - \sigma_2) + \ldots \frac{\alpha_m}{E}(\sigma - \sigma_m) \tag{14}$$

$$\sigma_m < \sigma \leq \sigma_{m+1}$$

The plastic strain rate, therefore, is given by

$$\dot{\varepsilon}_p = \alpha_m \dot{\sigma}_e / E \tag{15}$$

Using equation (1) and recognizing that for uniaxial deformation, effective quantities are proportional to the uniaxial components, the function $f(\sigma_e)$ can be reduced to

$$f(\sigma_e) = \alpha_m / E\sigma_e \tag{16}$$

The function is only linearly dependent on the current slope of the uniaxial curve. By specifying enough segments, virtually any hardening behavior can be accurately described.

Equations (1), (8) and (9) provide the fundamental relationships between stress and strain rates. The equilibrium conditions (governing equations) for a continuum body in the absence of body forces and inertia effects can be written as

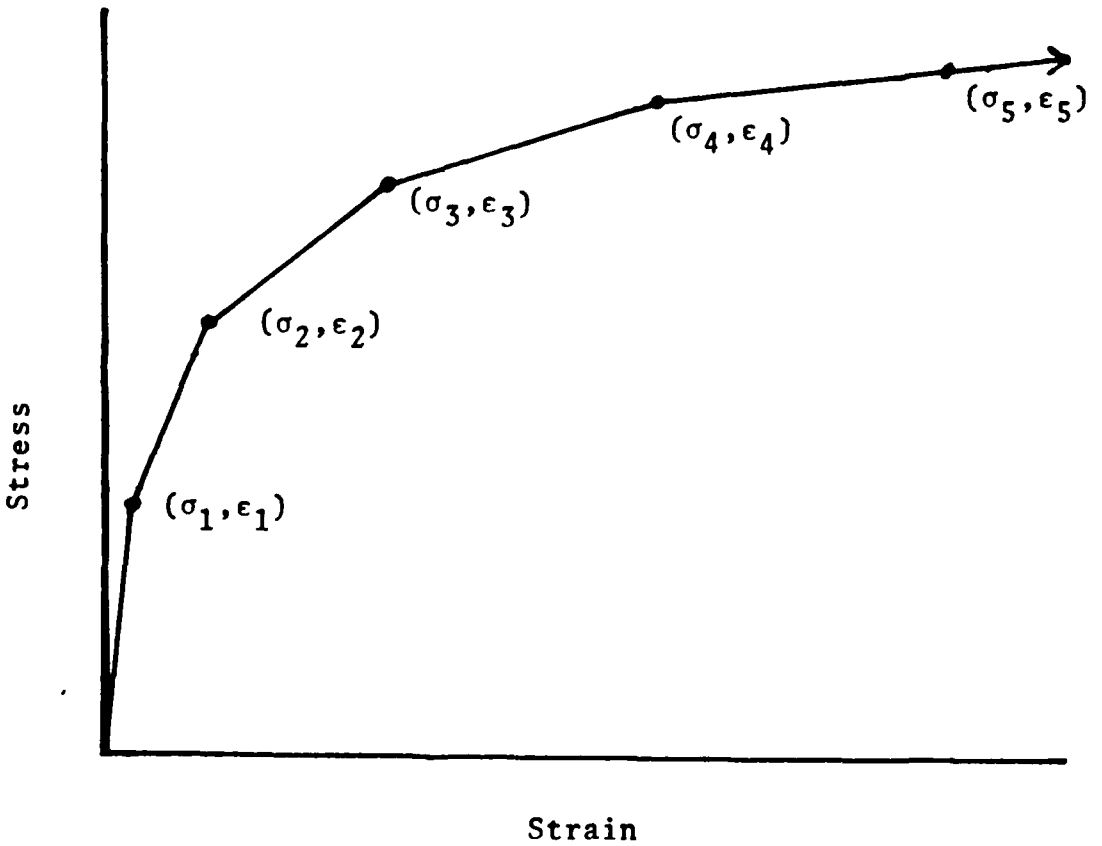

Figure 3: Multilinear Approximation For A Uniaxial Stress-Strain Curve With Hardening.

$$\partial \dot{\sigma}_{ij} / \partial x_j = 0 \tag{17}$$

with the boundary conditions

$$\dot{\sigma}_{ij} n_j = \dot{T}_i \text{ on } S_T$$

and (18)

$$\dot{u}_i = \dot{\overset{\cdot}{u}}_i \text{ on } S_u$$

where $\dot{T}_i$ are the specified loading rates on the boundary experiencing applied tractions (S_T) and $\dot{\overset{\cdot}{u}}_i$ are the velocities specified on the remainder of the boundary (S_u).

Equation (13) provides the fundamental relation between the stress state and the deformation gradients. For many problems in application the assumption of "small strain" introduces minimal error (mathematically, this means assuming infinitesimal displacements and strains). If this assumption is made, the strain rates are related to the velocity gradients by

$$\dot{\epsilon}_{ij} = \frac{1}{2}(\partial \dot{u}_i / \partial x_j + \partial \dot{u}_j / \partial x_i) \tag{19}$$

This simplification also means that the reference coordinate system and the material coordinate system are coincidental throughout the deformation. In the computer code described, the option of finite or infinitesimal strain theory is left to the user. The use finite strains slows convergence considerably for problems where the deformations are small. As the strains grow, however, the solutions assuming infinitesimal theory diverge from the finite strain results. Eventually infinitesimal solutions will fail to converge regardless of how small the load increments are taken.

By either employing the Principle of Virtual Work for increments of displacement or by performing the standard Galerkin technique on the governing equations, (17) and (18), the finite element equations governing the nodal velocities, $\dot{\underset{\sim}{U}}$, can be written in terms of the loading rate vector, R, in the form

$$\underset{\sim}{K}(\underset{\sim}{U}) \cdot \dot{\underset{\sim}{U}} - \dot{\underset{\sim}{R}} = 0 \qquad (20)$$

The standard finite element assumptions made are given by

$$\underset{\sim}{u} = \underset{\sim}{N} \cdot \underset{\sim}{U}$$

$$\dot{\underset{\sim}{\varepsilon}} = \underset{\sim}{B} \cdot \dot{\underset{\sim}{U}} \qquad (21)$$

$$\dot{\underset{\sim}{\sigma}} = \underset{\sim}{D}(\underset{\sim}{U}) \cdot \dot{\underset{\sim}{\varepsilon}}$$

$$K(U) = \sum_{\text{elements}} \int_{\text{element volume}} \underset{\sim}{B}^T \underset{\sim}{D}(\underset{\sim}{U}) \underset{\sim}{B} \, dV$$

where $\underset{\sim}{N}$ are the shape functions. The set of rate equations (20) will be integrated one load increment ($\Delta\underset{\sim}{R}$) at a given time to determine the corresponding new displacement increment, $\Delta\underset{\sim}{U}$. The Newton-Raphson or tangent stiffness solution procedure is employed. At load increment $L + 1$, the initial solution $\Delta\underset{\sim}{U}^i_{L+1}$ is found from

$$\underset{\sim}{K}(\underset{\sim}{U}_L) \cdot \Delta\underset{\sim}{U}^i_{L+1} = \Delta\underset{\sim}{R}_{L+1} \qquad (22)$$

The "new" displacement is then used in the stiffness matrix,

$K(U_L + \sum_{i=1}^{m} \Delta U^i_{L+1})$, and a new correction is obtained from

$$\underset{\sim}{K}\left[U_L + \sum_{i=1}^{m} \Delta U^{i}_{\sim L+1}\right] \cdot \Delta U^{m+1}_{\sim L+1} + \Delta R_{\sim L+1} -$$

$$U_L + \sum_{i=1}^{m} \Delta U^{i}_{L+1} \qquad (23)$$

$$\int_{U_L} \underset{\sim}{K}(U)\, d\underset{\sim}{U} = F^{i+1}_{\sim L+1}$$

where the integral is approximated using Simpson's rule. The procedure is repeated until two convergence criteria are met:

$$\left|F^{i+1}_{\sim L+1}\right|^2 / \left|\Delta R_{\sim L+1}\right|^2 \leq C_1$$

and (24)

$$\left|F^{i+1}_{\sim L+1}\right|^2 / \left|R_{\sim L+1}\right|^2 \leq C_2$$

where $R_{\sim L+1}$ is the total load at step L + 1.

In this study, 20-node quadratic isoparametric elements were employed exclusively. All integration was carried out utilizing 3 x 3 x 3 Gauss-Legendre quadrature formulae. Strains were calculated at the Gauss integration points in each element from the strain-displacement relations of (19). Stresses were cumulatively calculated at the Gauss points from the stress-strain relations.

Directly calculating strains and stresses from the finite element relations (21) at points on element boundaries inherently yields poor results. This is especially true when C^0 shape functions are employed. A superior approach is to calculate the stresses and strains at the Legendre quadrature points and to extrapolate or smooth them to the boundaries. This approach has been shown to yield very accurate results for a wide variety of geometric mappings. In this study the smoothing technique as developed in [6] is employed for all stress and strain evaluations.

For elastic-plastic studies, the authors prefer to model the crack front region with a convergent mesh of conventional elements rather than to employ a "singular" element. Experience with both elastic and elastic-plastic studies [3,7] demonstrates this approach to be accurate (although, for elastic problems, more costly). Since the nature of the singularity is unknown in the elastic-plastic problem, it is presumptuous to employ a singular element and may lead to erroneous results.

PROBLEM DESCRIPTION

Consider a panel of overaged 7075 (T7651) aluminum with a central through the thickness crack. A typical panel is shown in Figure 4. The panel used in this study had a width of 8.89cm and a crack length to width ratio of 0.5. The specimen thickness was 0.984mm and the specimen length was 17.78cm. The uniaxial stress-strain curve for the material is shown in Figure 5. The metallurgical aspects of this material and its ductility are discussed in a subsequent section.

Since the panel was loaded normal to the crack only, symmetry allowed the modeling of one octant. The finite element grid used in this study is shown in Figures 6a, 6b and 6c. The smallest elements near the crack front had planer dimensions of a/20 (where a is the half length of the crack). The convergence of this grid is discussed in [3,7].

The grid shown consists of 96 20-node isoparametric elements with 624 total nodes. The total grid has 1872 degrees of freedom. The system was solved by the frontal method. The total storage required for the entire program was 2.2 Megabytes (for double precision computations). Total runtime for the problem discussed was 48CPU Hours on a VAX 11/780.

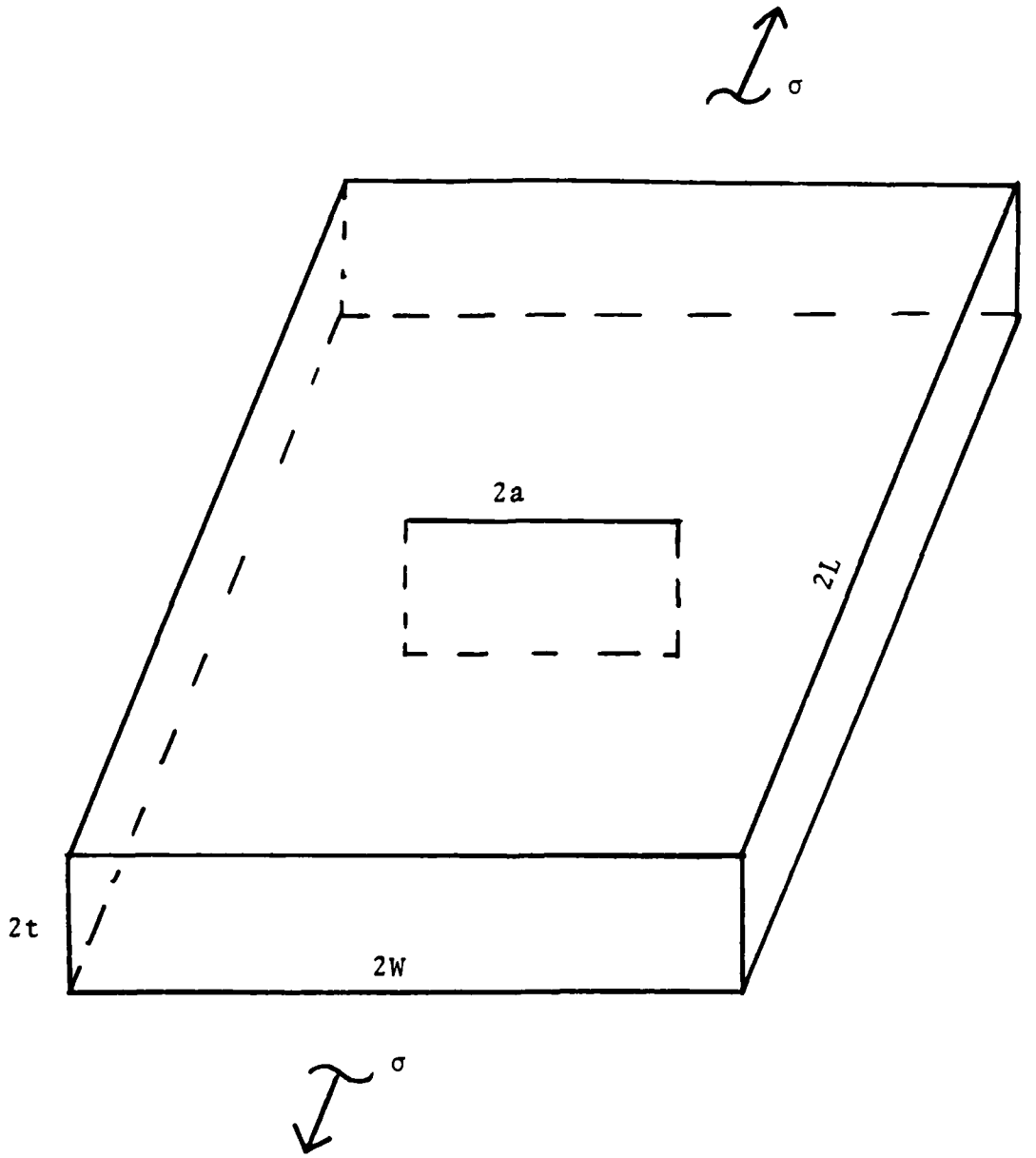

Figure 4: Typical Center Cracked Panel.

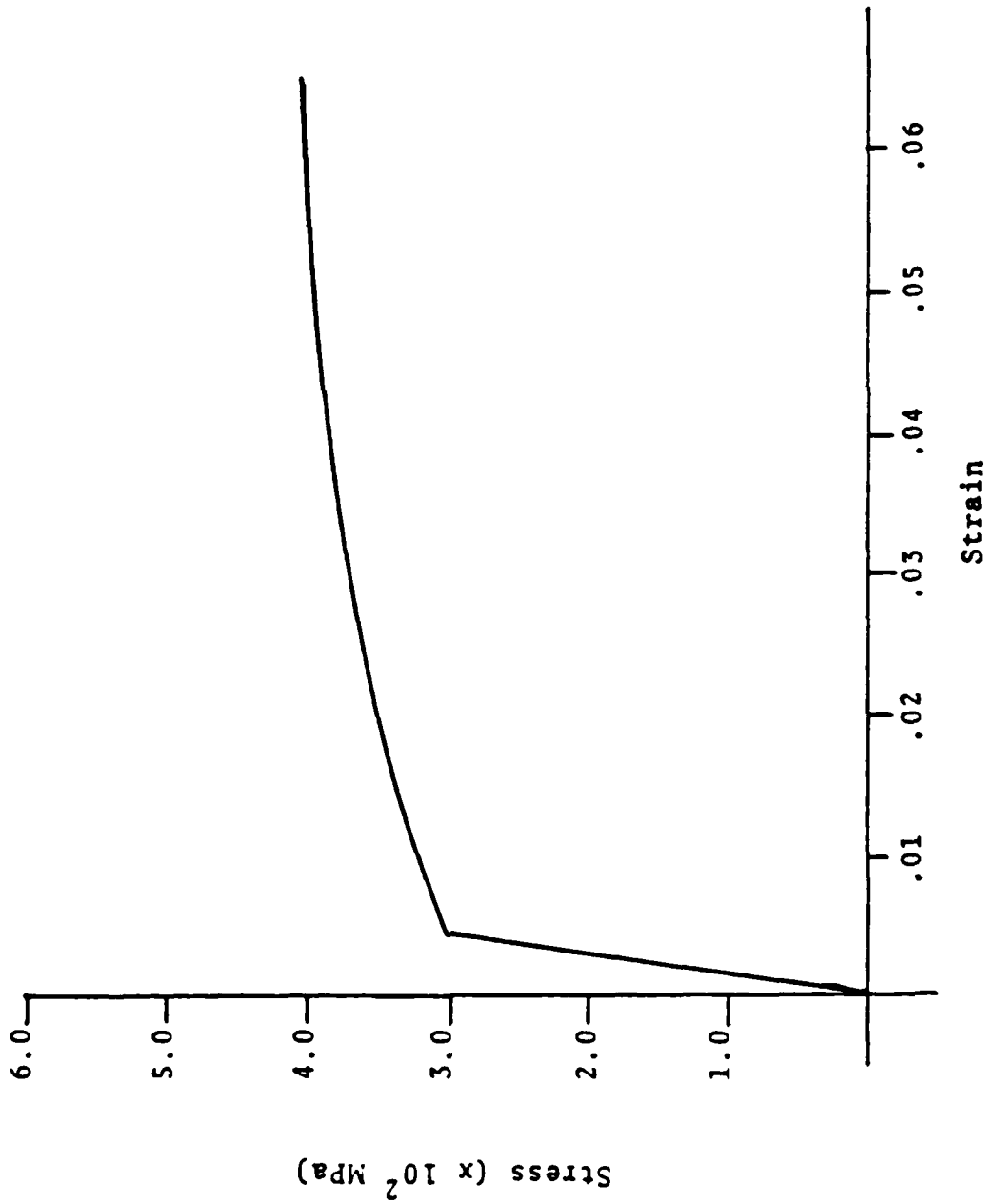

Figure 5: Uniaxial Stress-Strain Curve.

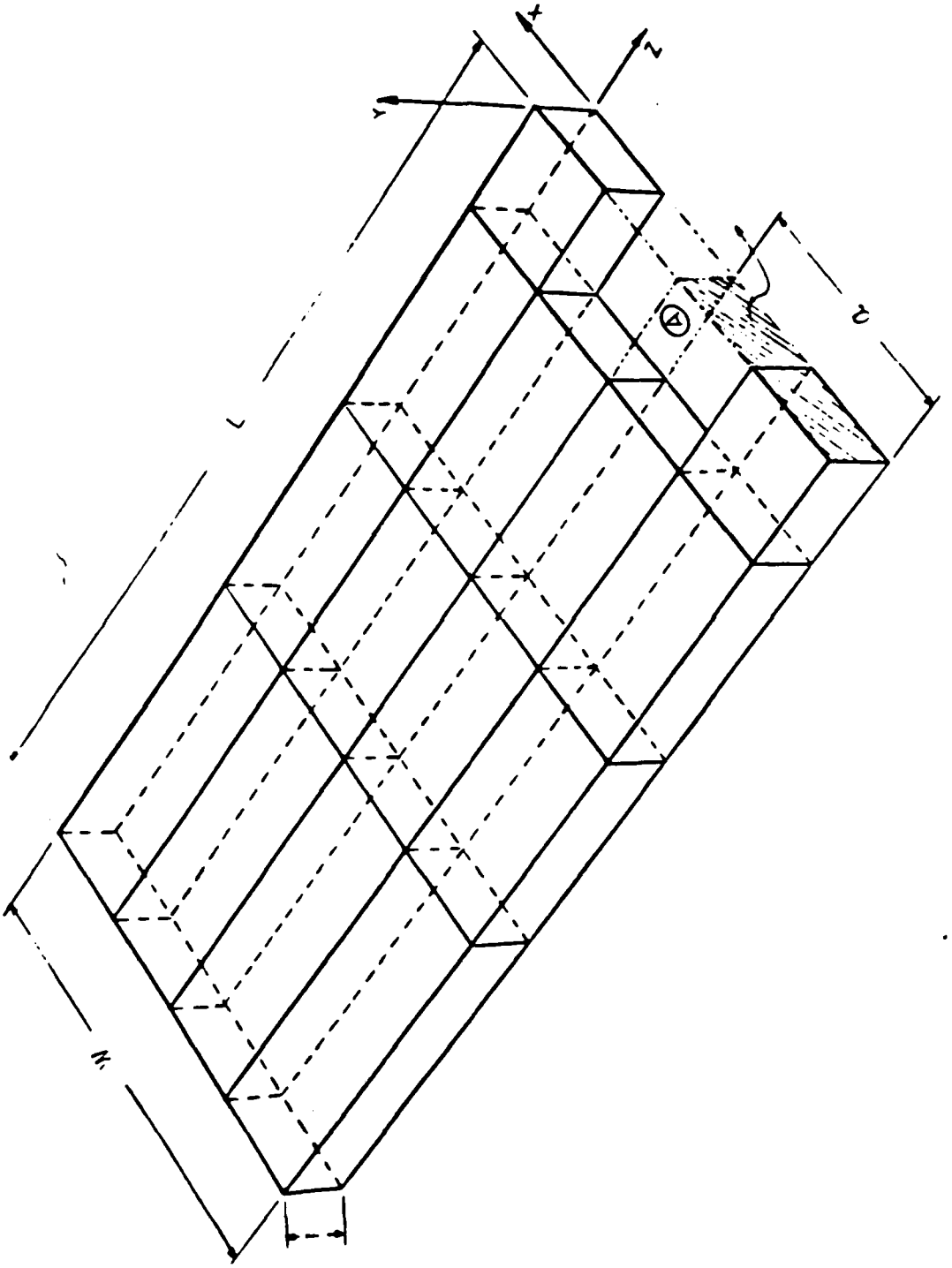

Figure 6a: Finite Element Grid - Coarse Outer Region.

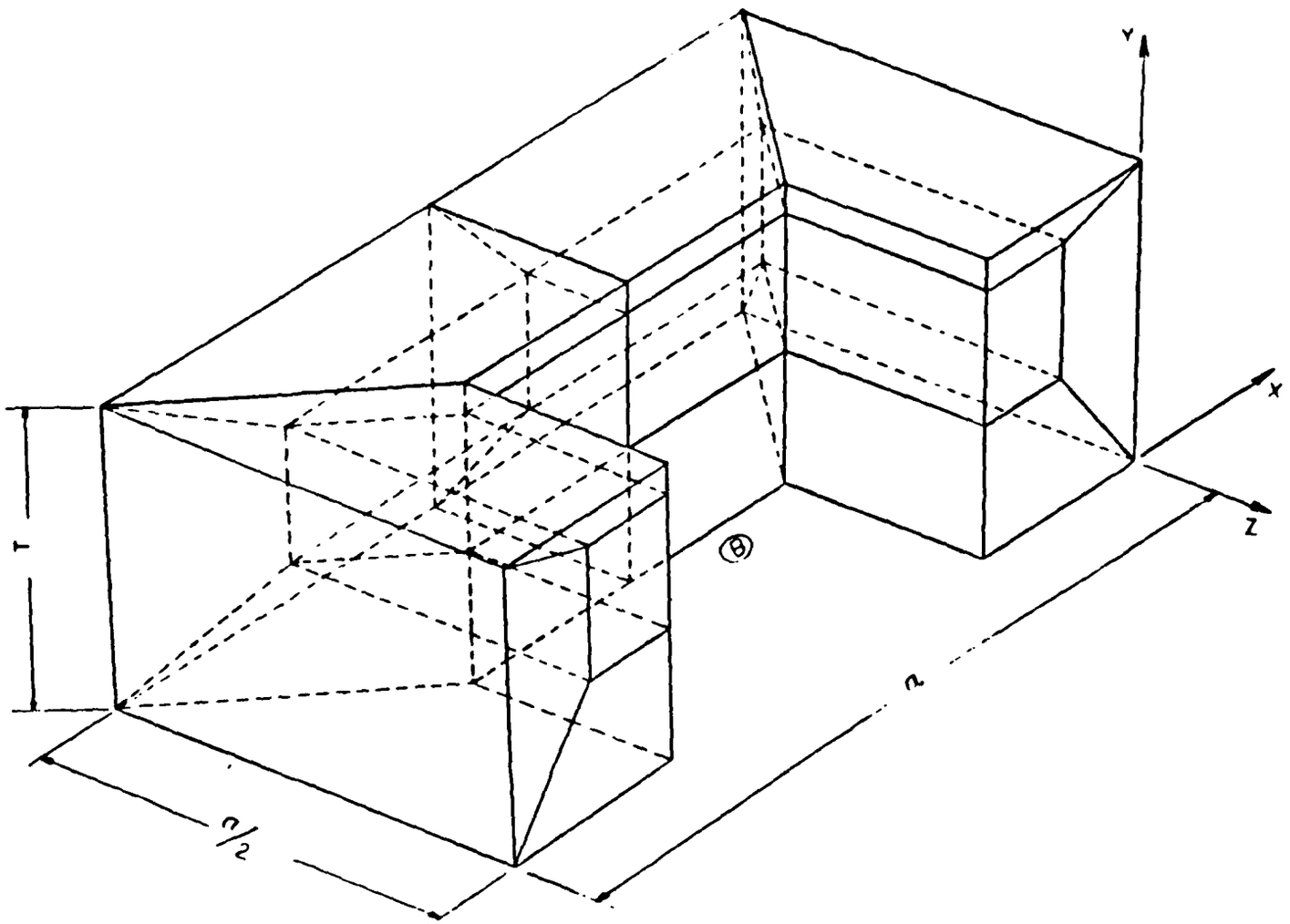

Figure 6b: Finite Element Grid - Blowup Of Region A.

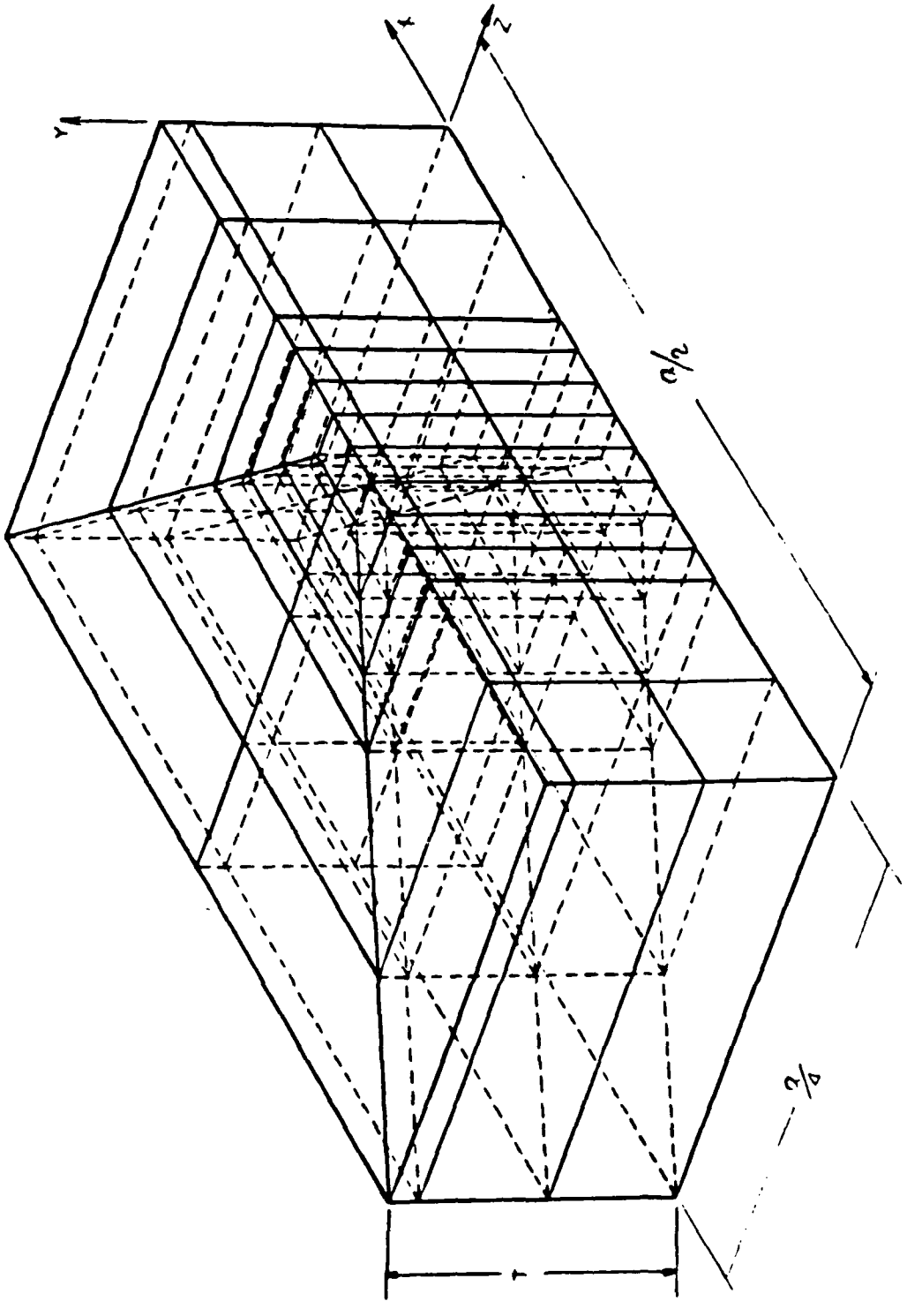

Figure 6c: Finite Element Grid - Near Tip Region B.

EXPERIMENTAL PROCEDURE

The ease and accuracy of measurement of the crack tip plastic zone shape will be high if the plastic zone is very large. This would require a material in a very ductile condition. However, such high ductility would create a large curvature in the crack front during fatigue precracking and difficulties in obtaining convergence in finite element analysis. Hence, an alloy in a moderately ductile condition was found to be desirable. These conditions were obtained in 7075 aluminum alloy by overaging from the T651 condition for 72 hours at 178°C (352°F). In this T7651 condition the alloy had a yield strength of 307MPa and ultimate tensile strength of 407MPa.

The specimen geometry used for this study was the center-cracked type with width, w = 89mm and crack length, 2a = 44.5mm. Fatigue cracks were initiated and extended from machined notches to obtain sharp crack tips. The fatigue precracking was performed at a load at least 50% lower than the load applied for plastic zone formation. After the fatigue crack was grown, the specimen was loaded to a desired load value to produce plastic zones at crack tips. The maximum load was limited by the load needed for crack growth initiation, as the experimental results were to be compared with the results of finite element analysis without crack

extension. Attempts were made to obtain as large a plastic zone as possible without crack growth; hence, the selected load was very close to that needed for stable crack growth initiation. Although initiation of stable crack growth is generally accompanied by a sudden drop in the load, in ductile materials, this drop is not easily detectable. Hence, to assure that no crack growth took place during loading, the specimen was fatigue cracked again after plastic zone size measurement to extend the crack approximately 2.5 to 5mm. The specimen was then loaded to fracture. If crack growth occurred during initial loading for formation of the plastic zone, the crack growth region would be marked by a dull appearance, distinguishing it from the fatigue crack growth region on either side. The results from such specimens were rejected.

The plastic zone size was determined by measuring the permanent reduction in thickness after the specimen was initially loaded and unloaded. The contours of the plastic zones were measured using a surface profile measuring device. The sensor of the device consisted of a pointer with a small tip radius attached to one end of a thin hardened titanium alloy sheet that was 51mm long, 19mm wide and 1.3mm thick. The other end of the sheet was rigidly mounted by sandwiching between two aluminum pieces. Two strain gauges of resistance 120ohms were mounted on each face of the titanium alloy

sheet. These strain gauges formed four arms of a Wheatstone bridge circuit. The circuit was similar to those used in load cells, extensometers and clip gauges. The output from the circuit was proportional to the movement of the pointer. The signal was amplified using a D.C. conditioner. The use of the thin titanium alloy sheet reduced the pressure on the specimen by the pointer, and scratching of the surface was minimized.

The specimen was mounted horizontally on a table with two micrometer screw feeds at right angles to each other. The specimen was mounted in such a way that the direction of crack (x-direction) was parallel to the direction of traverse of one micrometer screw. When the sensor was mounted the pointer was pressing against the specimen vertically. The specimen was moved underneath the sensor using the micrometer screw-feeds. The output from the sensor was used to drive the x-axis of an x-y recorder. The y-direction displacement of the table was measured using an extensometer attached to the system, and the output from the extensometer was used to drive the y-axis of the x-y recorder. Several traverses in the y-direction were made for each face of the specimen at regular intervals of distance from the crack tip in the x-direction. The curves obtained from these traverses were used to establish points around the crack tip corresponding to a given thickness reduction. From these, contour lines for different thicknesse. were established. This process was repeated for all the four faces of the specimen.

EXPERIMENTAL RESULTS

The contour lines delineate the size and shape of the plastic zone. The thickness of the specimen falls between those required for plane stress and plane strain conditions. The plastic zones obtained had a shape representative of this thickness range.

A set of contour lines obtained from one face of the specimen are shown in Fig. 7. The scatter in the data for the outer contour lines is higher than the inner ones. This is because the rate of thickness variation decreases with increasing distance from the cracked tip, as can be seen from the differences in the spacings between adjacent contour lines. Although the resolution of the sensor is very high and is limited only by the extent of the amplification of the signal, errors can be introduced due to any nonplanarity of the initial specimen surface and slight variations in the pressure applied on the micrometer screws while advancing manually. The planarity of the surface was checked initially before deforming the specimen. The variations in pressure can cause an error of approximately 0.0025mm. The depth of 0.0051mm and 0.0102mm represented by the outer contour lines are very sensitive to these variations. The scatter in the data, also is produced by the nonhomogeneity of the material, caused by coring and inclusions during casting and orientation effects during subsequent mechanical processing.

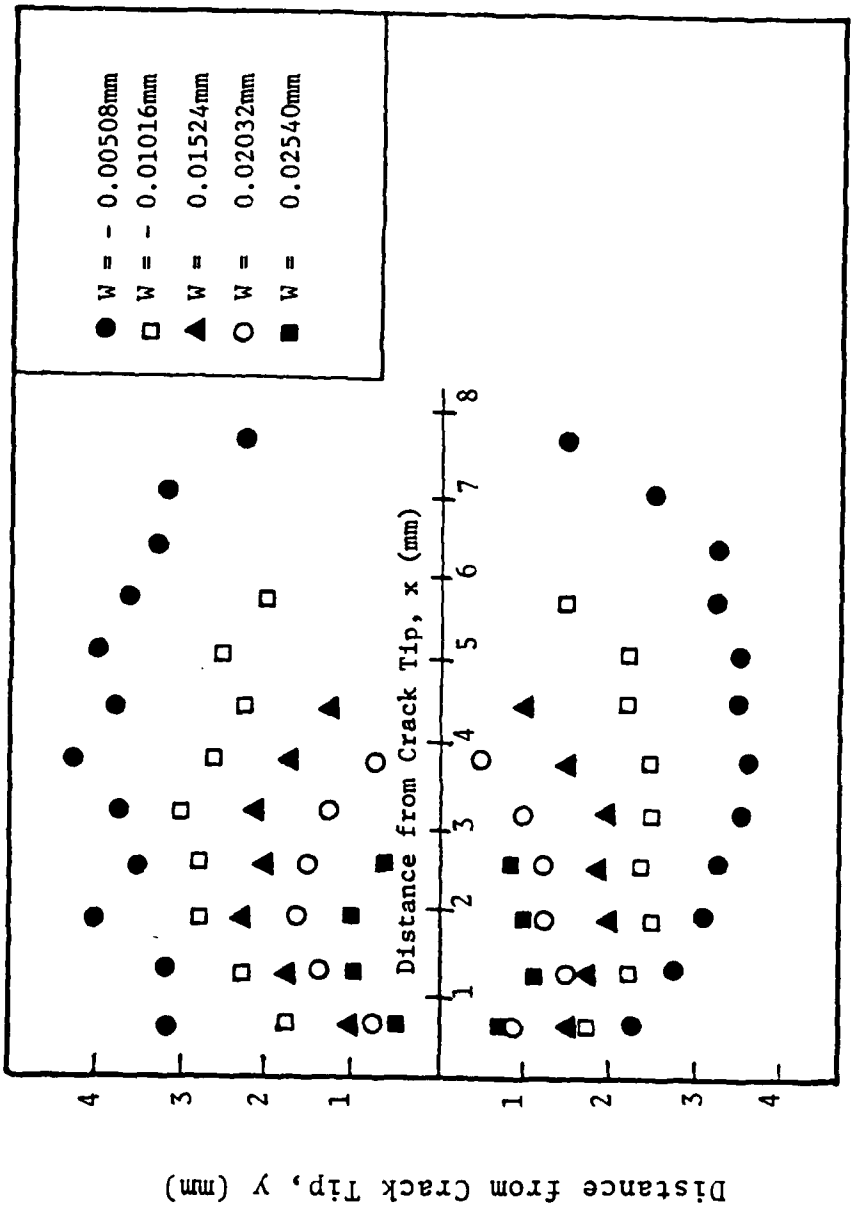

Figure 7: Surface Displacements Near a Crack Tip.

It is also seen that the plastic zone is not exactly symmetrical to the initial notch direction, which also can be attributed to inhomogeneity. Plastic deformation occurs more extensively in the softer regions. Material inhomogeneity also may cause change in the orientation of the fatigue crack, which tilts the zone ahead of it. Nonsymmetry can also be produced by misalignment of the specimen and the testing machine, but the misalignment in the set up used was negligible.

In the finite element analysis inhomogeneity is not taken into consideration and hence, the zone is assumed to be symmetrical. A comparison with the finite element results can be made by averaging the distance of each set of contour lines from the initial notch direction. Such contour lines determined from the four faces are shown in Figs. 8-11. The zone sizes are slightly different for the four faces. This also results from the uneven crack growth during fatigue cracking due to inhomogeneity. Since the excess deformation in one region is compensated by the lack of it in another, averaging the results minimizes the error involved.

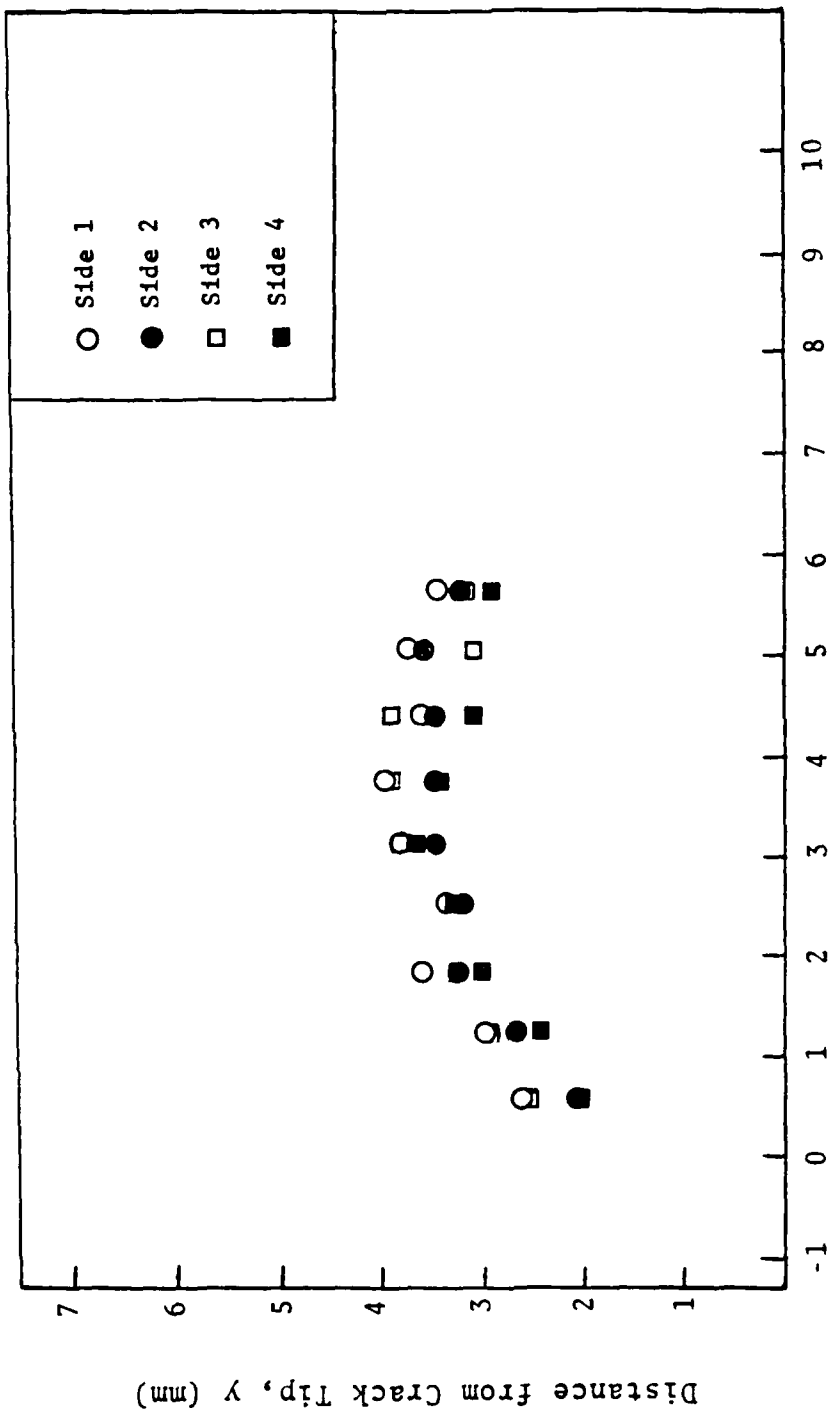

Figure 8: Contour Lines of Depth, 0.00508mm.

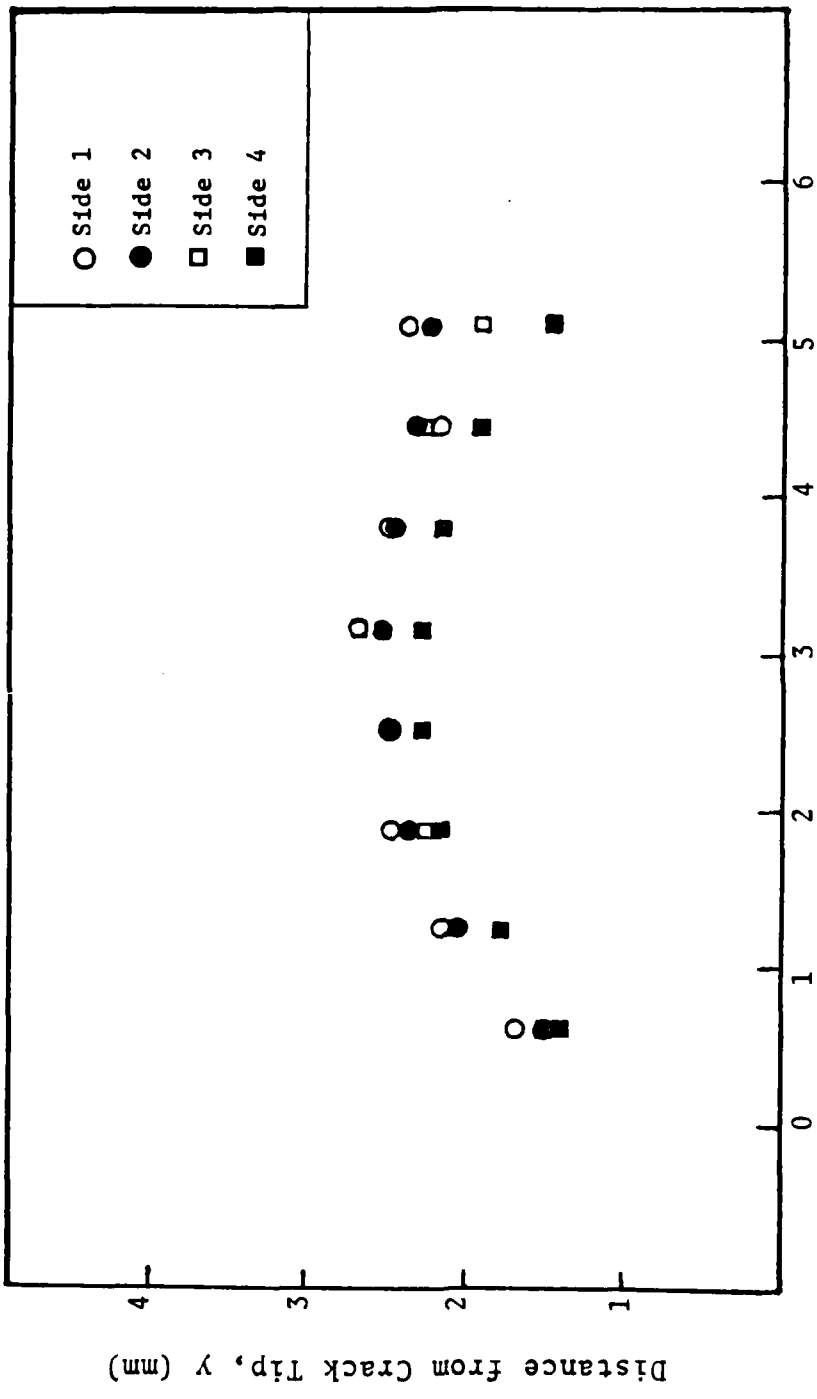

Figure 9: Contour Lines of Depth, 0.01016mm.

Figure 10: Contour Lines of Depth 0.01524mm.

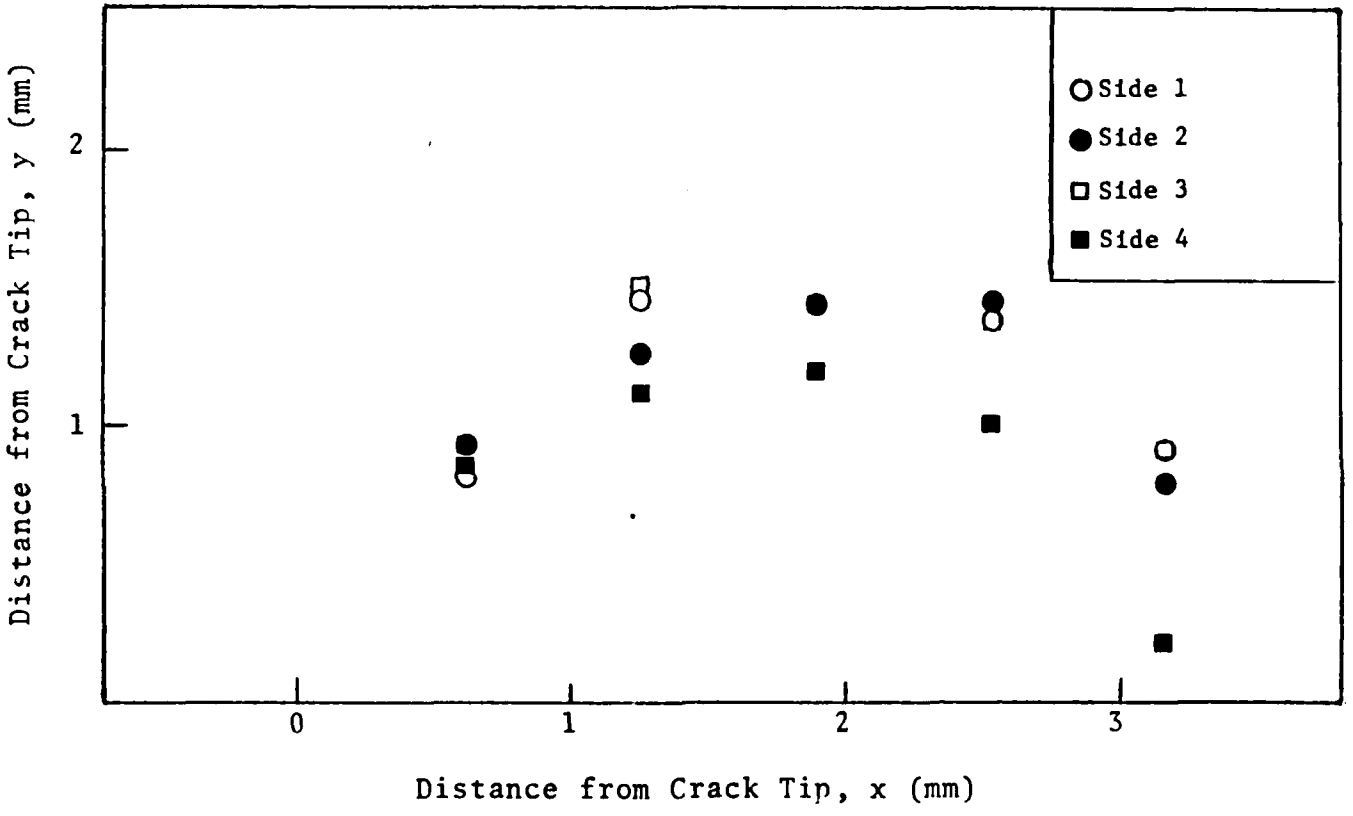

Figure 11: Contour Lines of Depth 0.02032mm.

COMPARISON EXPERIMENTAL AND FINITE ELEMENT RESULTS

The finite element analysis discussed previously was performed and the residual deformation after unloading the specimen was calculated. These results were plotted as contraction contours and are shown in Fig. 12. The average results (the average of all four sides as previously discussed) are also plotted from the experiment. The results from the finite element analysis are in good agreement with those obtained from the experiment.

The finite element predicts slightly more plasticity than the experiment predicts. This is expected since the finite element formulation assumes all nonlinearity is due to plastic (or permanent) deformation. In real materials, however, there is some recoverable nonlinear deformation (i.e., nonlinear elastic deformation). The averaging, material inhomogeneity and error in the two methods more than account for the deviations (less than 4%, maximum).

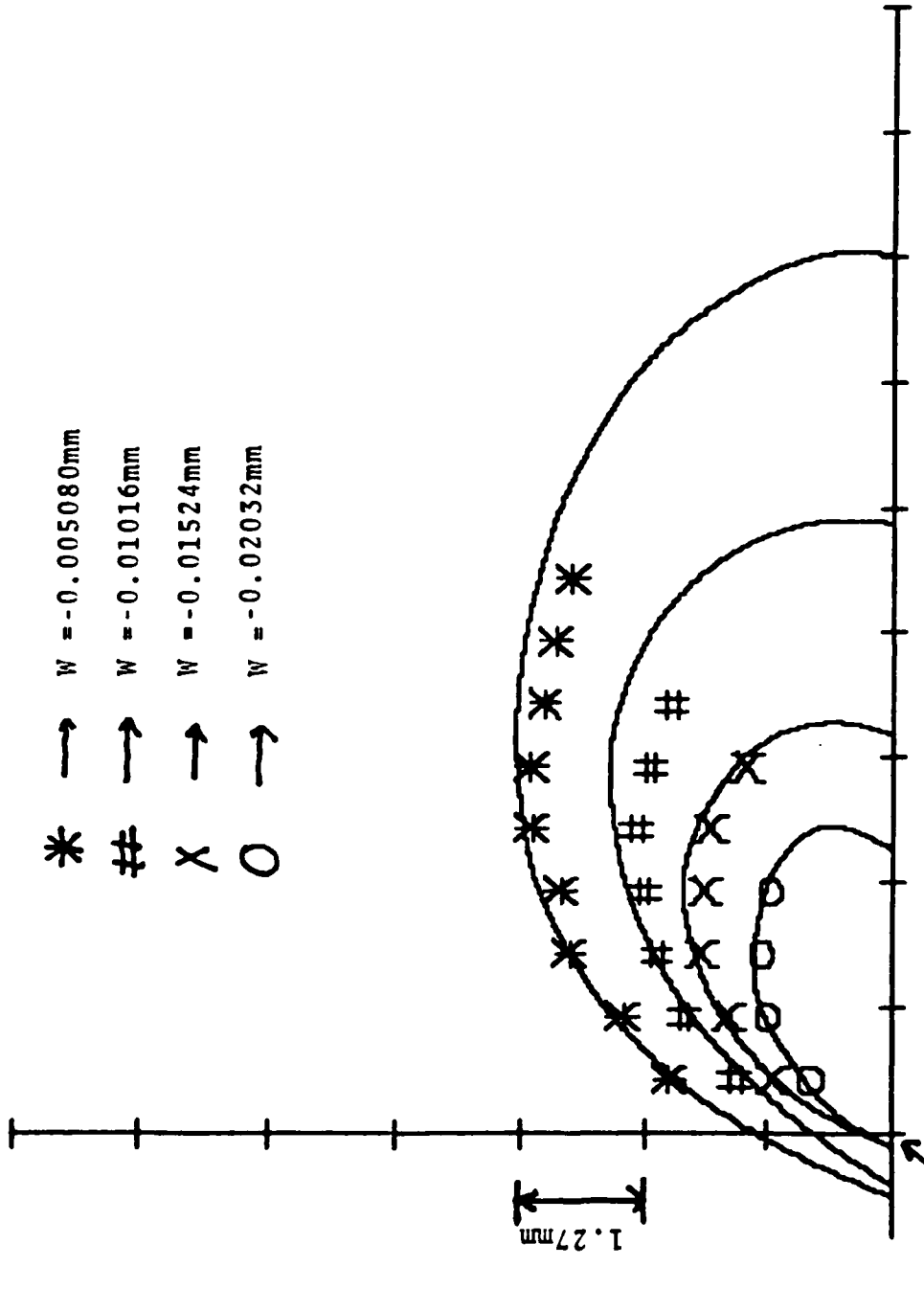

Figure 12: Comparison of Surface Displacements.

CONCLUDING REMARKS

Comparison was made between the experimental and finite element surface contractions for a center-cracked panel. The results compare favorably indicating the accuracy and realistic modeling of this finite element formulation and modeling. The deviations between the results which were observed are less than can be accounted for due to inherent error in the measurements. In fact, the results are more accurate than one would expect.

It is important to highlight several factors when discussing three dimensional finite element analyses in general, and in particular for nonlinear problems. The results are highly dependent on the grid characteristics and on the convergence algorithm employed. Additional degrees of freedom do not guarantee a more accurate solution [1,2,3]. When employing three dimensional finite element models, convergence studies alone are not sufficient. Comparison between predictions and true material behavior is essential. With regard to fracture problems, it is essential to compare predictions from analysis with local parameters as erroneous local models can be forced to produce results which agree globally (i.e., on remote quantities, e.g., nonlinear compliance).

The unique aspect of the study presented in this paper is the direct comparison with experimentally measured local quantities demonstrates the accuracy of the modeling employed. This approach can now confidently be applied to fracture problems for the testing of fracture criteria and the prediction of crack growth and instability. Without such a demonstration, numerical solutions and verification of failure criteria are always suspect. Due to the complicated nature of the problem, each component of the analysis must be verified independently to guarantee accurate solutions and meaningful predictions. This component is lacking in three-dimensional studies reported to date.

ACKNOWLEDGEMENT

This work was sponsored by the Office of Naval Research under Contract Number: N00014-84-K-0027.

REFERENCES

1] E. Thomas Moyer, Jr. and H. Liebowitz, "Plastic Deformation and Hardening Characteristics in Three-Dimensional Fracture Specimens. Presented at the ICF International Symposium on Fracture Mechanics (Proceedings published in China Science Press), Beijing, China, November 22-25, 1983.

2] E. Thomas Moyer, Jr. and Harold Liebowitz, "Effect of Specimen Thickness on Crack Front Plasticity Characteristics in Three-Dimensions." Presented at the Sixth International Conference on Fracture, New Delhi, India, December 4-10, 1984.

3] E. T. Moyer, Jr. and H. Liebowitz, "Finite Element Methodology for Elastic-Plastic Fracture Problems in 3-Dimensions." To appear in the commemorative issue of the Journal of Numerical Methods in Engineering in memory of Bruce Irons, 1985.

4] R. Hill, The Mathematical Theory of Plasticity, Oxford University Press, London, 1956.

5] S. W. Key, "A Finite Element Procedure for the Large Deformation Dynamic Response of Axisymmetric Solids." Computer Methods in Applied Mechanics and Engineering, Vol. 4, pp. 195-218, 1974.

END

FILMED

8-85

DTIC